Digital Adaptive Optics: Introduction and Application to Anisoplanatic Imaging

Mathieu Aubailly and Mikhail A. Vorontsov

Additional information is available at the end of the chapter

1. Introduction

1.1. Conventional adaptive optics

Adaptive optics (AO) was originally developed for astronomical applications and aims to compensate the degrading effect of atmospheric turbulence on optical imaging systems performance [1]. It was later adapted to other applications such as free-space laser communication, surveillance, remote sensing, target tracking and laser weapons [2]. It also found applications in the medical field with retinal imaging [3] and potentially laser surgery. While in the later case degradations are induced by the Earth atmosphere, ocular aberrations are the limiting factor in the latter case.

Regardless of the application of interest, conventional AO systems typically perform two tasks: (1) they sense the wavefront aberrations resulting from wave propagation through the random media (e.g. the atmosphere), and (2) they compensate these aberrations using a phase conjugation approach. The components required to perform these tasks typically consist of a wavefront sensor (WFS) such as the widely-used Shack-Hartmann WFS, a wavefront corrector (WFC) – typically a deformable or segmented mirror – and a control device that computes the actuator commands sent to the WFC from the WFS data. This compensation process must be performed at speeds that match or exceed the rate of evolution of the random media – so-called real-time compensation. As a result of this requirement conventional adaptive optics systems are usually complex and often costly.

Although the conventional AO approach successfully mitigates turbulence-induced wavefront phase aberrations it presents fundamental and technological limitations.

INTECH
open science | open minds

1.2. Limitations of conventional adaptive optics

Performance of AO systems is limited by a number of factors among which wavefront correctors performance have a strong impact. First, WFC's have a limited number of degrees-of-freedom. For example, the number of control channels of a deformable mirror seldom exceeds a few tens across its aperture. This limitation affects the spatial scale of the wavefront features the WFC can compensate and prevents the system from mitigating high-order aberrations (i.e. aberrations with small spatial features). This constrain is especially critical for optical systems with aperture diameter $D \gg r_0$, where r_0 is the Fried parameter [4]. Another restrictive feature of WFC's is the limited amplitude of the wavefront phase they can compensate. This limitation prevents in parts conventional AO systems to be effective under strong (deep) turbulence conditions, which are typical for optical systems operating over long and/or near-horizontal (slant) atmospheric propagation paths. Finally, the limited temporal response of WFC's may prevent them from providing compensation at rates that exceed the rate of aberration changes.

Although technological developments have been providing WFC's with higher spatial resolution, increased dynamical range and bandwidth, an effect known as anisoplanatism which is reviewed briefly in the next section remains a fundamental limitation for adaptive optics compensation.

1.3. Anisoplanatism

Conventional AO systems typically require a reference beam (guide star) that is used to probe the atmospheric turbulence and provide an optical signal to the WFS [5]. However, the light arising from different directions within the scene does not experience the same atmospheric turbulence aberrations (propagation through volume turbulence) [6]. This causes AO performance to vary spatially across the field-of-view (FOV) with best image quality achieved for directions near the reference beam and over a small angular subtense in the order of the isoplanatic angle θ_0 [7]. The isoplanatic angle depends on the turbulence strength profile $C_n^2(z)$ where z is the altitude, and is given by

$$\theta_0 = \frac{58.1 \times 10^{-3} \lambda^{6/5}}{\left[(\sec \theta_z)^{8/3} \int_0^L C_n^2(z) z^{5/3} dz \right]^{3/5}}, \qquad (1)$$

where θ_z is the Zenith angle of observation and λ is the wavelength [4]. Even under conditions of weak turbulence θ_0 is usually small and remains in the order of a few microradians to a few tens of microradians. The isoplanatic angle is especially narrow for near-ground and near-horizontal propagation paths (i.e. high and nearly constant C_n^2 values). Anisoplanatism degrades the performance of AO systems as the angular separation θ (known as field angle) between the reference beam and points on the object increases [8].

A number of techniques have been developed to mitigate the effect of anisoplanatism such as using multiple WFS's and WFC's located in optical conjugates of planes at various distan-

ces along the light of sight – an approach referred to as multi-conjugate AO (MCAO) [9-11]. Using multiple guide stars distributed within the field-of-view has also been explored [12]. Although these approaches have been shown to be effective, they both result in significant increase of system complexity and cost. Post-processing techniques have been investigated but they usually assume knowledge of the point spread function (PSF) for several values of the field angle θ [13].

In the remainder of this chapter we introduce an alternative approach to conventional adaptive optics – referred to as digital adaptive optics (DAO) – which alleviates the need for physical WFC devices and their corresponding real-time control hardware, and relieves the system from the limitations associated to them (see section 1.2). In section 2 we present the approach used in DAO systems and discuss their limitations. The DAO technique is then applied to an anisoplanatic imaging scenario and results of numerical analysis are presented in section 3. Finally section 4 draws conclusions.

2. Digital adaptive optics

2.1. General approach

The notional schematic in Figure 1 shows the sequential steps required for obtaining a compensated image using the digital adaptive optics approach. Two major steps of the process are as follow:

Step 1: Optical field measurement

The front-end of the DAO system consists of an optical reducer and an optical sensor referred to as complex-field sensor (CFS). The CFS provides simultaneous measurements of the optical field wavefront phase and intensity distributions in its pupil plane, denoted $\varphi(\mathbf{r})$ and $I(\mathbf{r})$ respectively. This sensor is referred to as a complex field sensor since the complex amplitude of optical field $A(\mathbf{r})$ can be represented in the form $A(\mathbf{r}) = |A(\mathbf{r})| \exp\{j\varphi(\mathbf{r})\}$, where $|A(\mathbf{r})| = I^{1/2}(\mathbf{r})$, and both phase $\varphi(\mathbf{r})$ and amplitude $|A(\mathbf{r})|$ functions can be obtained from the sensor measurements. The reducer is used for re-imaging of the DAO system pupil onto the CFS pupil so that $A(\mathbf{r}) \approx A_{in}(M\mathbf{r})$ where $A_{in}(\mathbf{r})$ denotes the complex amplitude of the optical field entering the DAO system. The term M is a scaling factor associated with the beam reducer and $\mathbf{r} = \{x, y\}$ designates a coordinate vector in the system pupil plane. To simplify notation, we assume $M = 1$ and $A(\mathbf{r}) \approx A_{in}(\mathbf{r})$. Section 2.3 provides details about complex field sensing techniques for DAO systems.

As a result of propagation through atmospheric turbulence the wavefront phase $\varphi_{in}(\mathbf{r})$ received at the DAO system's pupil (and measured by the CFS sensor) can be separated into two components:

$$\varphi_{in}(\mathbf{r}) = \varphi_{obj}(\mathbf{r}) + \varphi_{turb}(\mathbf{r}) \tag{2}$$

where $\varphi_{obj}(\mathbf{r})$ is the phase component related to the object of interest (scene) and $\varphi_{turb}(\mathbf{r})$ is the turbulence-induced phase term which needs to be compensated. The second step of the DAO process aims to (1) compensate phase aberrations $\varphi_{turb}(\mathbf{r})$ which degrade the quality of the images produced by the system and (2) preserve phase $\varphi_{obj}(\mathbf{r})$ which is used to synthesize a compensated image.
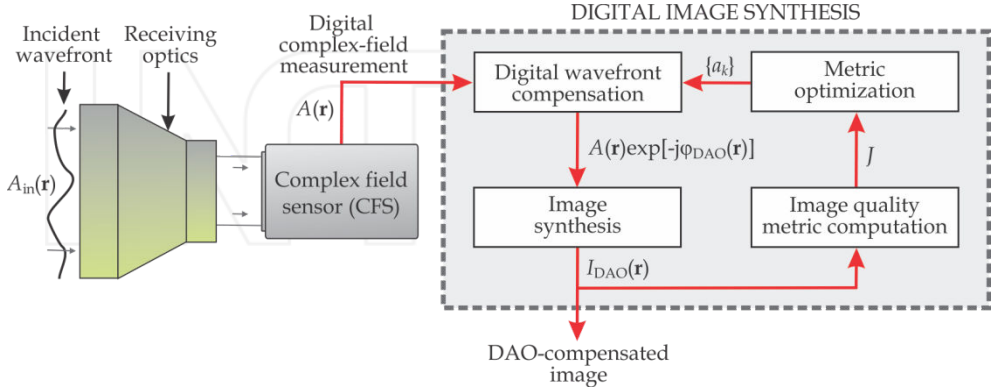

Figure 1. Notional schematic of a digital adaptive optics system.

Step 2: Digital image synthesis

In this second step of the DAO technique, a digital processing technique is used to synthesize a compensated image from the complex-field measurement $A(\mathbf{r})$ provided by the CFS (see step 1). As illustrated in Fig. 1 this step includes compensation of the measured complex field $A(\mathbf{r})$ using phase function $\varphi_{DAO}(\mathbf{r})$ and results in compensated field $A_{DAO}(\mathbf{r}) = A(\mathbf{r})\exp\{-j\varphi_{DAO}(\mathbf{r})\}$. This phase conjugation step using numerical phase function $\varphi_{DAO}(\mathbf{r})$ can be regarded as the digital equivalent of phase conjugation using a wavefront corrector such as a deformable mirror or a liquid crystal phase modulator which are used in conventional AO systems. We refer to this step as digital wavefront compensation (DWFC).

The compensated complex-field $A_{DAO}(\mathbf{r})$ is then used to synthesize image $I_{DAO}(\mathbf{r})$. Image quality of $I_{DAO}(\mathbf{r})$ hence depends on phase $\varphi_{DAO}(\mathbf{r})$ applied at the DWFC step. The quality of image $I_{DAO}(\mathbf{r})$ is assessed by computing an image quality (sharpness) metric J, and an algorithm is used to optimize metric J, leading to an image $I_{DAO}(\mathbf{r})$ with improved quality. Details about the image formation and optimization process are presented in section 2.4.

2.2. Comparison between conventional and digital AO system operations

For a conventional AO system to operate successfully wavefront compensation (conjugation) is required to be performed during time $\tau_{AO} < \tau_{at}$ where τ_{at} is the characteristic time of atmospheric turbulence change (i.e. under "frozen" turbulence conditions). Such a system is

referred to as *real-time* system and its temporal response results of the combination of the individual response time of each element of the AO feedback loop shown in Fig. 2(a) so that:

$$\tau_{AO} = \tau_{WFC} + \tau_{WFS} + \tau_{cont} \tag{3}$$

where τ_{WFC}, τ_{WFS} and τ_{cont} correspond respectively to the temporal response of the WFC, WFS and controller devices. Bandwidth requirements hence apply to each element of the feedback loop and drive in part the cost of AO systems.
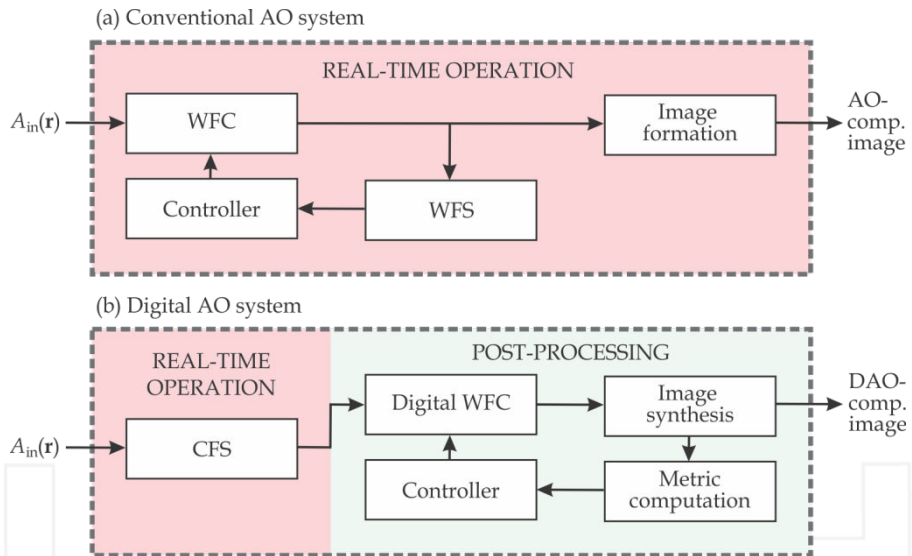
Figure 2. Block diagram identifying keys components of (a) a conventional AO system and (b) a digital AO system. While conventional AO requires both wavefront sensing and wavefront compensation to be performed in real-time, digital AO requires only complex-field sensing to be realized in real-time. Subsequent digital image formation and compensation can be performed as a post-processing step.

Although digital AO systems are based on the same principle of phase conjugation than conventional AO, compensation is implemented in a difference manner. DAO systems employ numerical techniques and do not use physical wavefront corrector devices such deformable or segmented mirrors. This has the advantage of alleviating the need for WFC's and their real-time control hardware, two elements that impacts significantly the cost and complexity of conventional AO systems.

In a DAO system measurements of the input complex-field $A_{in}(\mathbf{r})$ are performed during $\tau_{CFS} < \tau_{at}$ (i.e. in real-time) while image formation and compensation of turbulence-induced phase aberrations are performed as *post-processing* steps as illustrated in Fig. 2(b). Since the post-processing step is not required to be performed at high speed, it can be achieved using standard computation techniques such as a PC, which simplifies implementation of DAO systems. The time delay associated with image synthesis and compensation using such techniques may be suitable for some applications. However, for applications where real-time DAO operation is critical, the post-processing step may be implemented on a dedicated high-speed hardware.

2.3. Wavefront sensing techniques for DAO systems

In conventional AO systems the spatial resolution of the wavefront sensor output (i.e. the spacing between data points) is related to the spatial resolution of the wavefront corrector (e.g. spacing between deformable mirror actuators). Sensing of the incoming wavefront aberrations with high spatial frequency does not provide better AO performance if the corrector device is unable to match this spatial resolution. In the other hand image quality in DAO systems is directly related to the spatial resolution of the wavefront measurement. DAO systems hence require high resolution wavefront sensing capabilities.

Although the resolution yielded by wavefront sensors typically used in adaptive optics such as Shack-Hartmann [1,14] or curvature sensors [15,16] does not exceed a few tens to a couple hundred data points across the system's aperture, a number of wavefront sensing techniques capable of providing high resolution outputs exist. Among them some are potentially suitable for DAO systems including: phase retrieval from sets of pupil and focal plane intensity distributions [17-19], phase diversity [20,21], schlieren techniques and phase contrast techniques [22,23] such as the Zernike filter [24-26] and the Smartt point-diffraction interferometer [27-30]. Approaches based on holographic recording of the wavefront have also been used successfully [31-33]. The recently developed sensor referred to as multi-aperture phase reconstruction (MAPR) sensor [34] uses a hybrid approach between the Shack-Hartmann and Gerchberg-Saxton [17] techniques to provide high-resolution measurements and is also a candidate for DAO system implementation.

A growing number of applications now require operation over near-horizontal or slant atmospheric paths. These propagations scenarios are characterized by moderate to strong intensity scintillation [35-37]. This means that in addition to high resolution requirements, robustness to high scintillation levels is a critical criterion for selecting sen-

sors suitable for DAO applications. Another important criterion is the computational cost of the wavefront reconstruction algorithm as it impacts the speed of operation of the sensor. In this regard the MAPR sensor might be suitable for DAO applications since it is capable of providing high-resolution measurements under conditions of strong intensity scintillation (so called scintillation-resistant) and in the presence of branch points [38,39]. It yields an average Strehl ratio exceeding 0.9 for scintillation in-dex values $\sigma_I^2 \leq 1.25$ and $D/r_0 \leq 8$, and 0.8 for $\sigma_I^2 \leq 1.75$ and $D/r_0 \leq 12$ and reconstruction is computationally efficient as a result of the parallel nature of the algorithm.

However, as the selection of wavefront sensing techniques suitable for DAO-based imaging requires further investigations, we assume in the remainder of this chapter that the complex amplitude of the incident optical field $A_{in}(\mathbf{r})$ (see Fig. 1) is known and that $A(\mathbf{r}) = A_{in}(\mathbf{r})$. DAO image synthesis and compensation techniques based on measurement $A(\mathbf{r})$ are provided in the next section.

2.4. Anisoplanatic image synthesis and compensation

As a result of anisoplanatism (see section 1.3) image quality varies significantly across the field-of-view of the system and image compensation based on phase conjugation (section 2.1) is effective only over a small angular extent with size related to the isoplanatic angle θ_0. An approach for performing efficient DAO compensation is to apply the technique locally over image regions that are nearly isoplanatic. We present in this section a block-by-block (mosaic) post-processing technique in which the DAO approach is applied sequentially to regions (blocks) Ω_j and the resulting image consists in the combination of compensated im-age regions Ω_j into a single image corresponding to the entire FOV (region Ω). Consider an image region Ω_j defined by function

$$M_{\Omega_j}(\mathbf{r}) = \exp\left[\left(-\frac{|\mathbf{r} - \mathbf{r}_j|^2}{2\omega_\Omega^2}\right)^8\right], \tag{4}$$

where $\mathbf{r}_j$ defines the position of the jth image region and ω_Ω denoted its size. Image synthe-sis and DAO compensation over region Ω_j is performed based on the measurement $A(\mathbf{r})$ of the optical field in the pupil of the system and consists of the following steps:

Step 1: Digital wavefront correction

A wavefront corrector phase function $\varphi_{DAO}(\mathbf{r})$ is represented as

$$\varphi_{DAO}(\mathbf{r}) = \sum_{k=1}^{N_{DAO}} a_k S_k(\mathbf{r}), \tag{5}$$

where $\{S_k(\mathbf{r})\}$ is a set of response functions for the digital wavefront corrector, $\mathbf{a} = \{a_k\}$ is the vector of commands sent to the DWFC, and N_{DAO} is the number of control

channels of the DWFC. The corrector phase function $\varphi_{DAO}(\mathbf{r})$ is then applied to the complex field amplitude $A(\mathbf{r})$ provided by the CFS and results in compensated field $A_{DAO}(\mathbf{r})$ given by

$$A_{DAO}(\mathbf{r}) = A(\mathbf{r})\exp\left[-j\varphi_{DAO}(\mathbf{r})\right]. \tag{6}$$

Step 2: Image synthesis

The compensated field $A_{DAO}(\mathbf{r})$ in Eq. (6) is used for synthesis of the DAO compensated image $I_{DAO}(\mathbf{r})$. The DAO image is computed using the Fresnel approximation as follows [25]:

$$I_{DAO}(\mathbf{r}) = \left| \frac{1}{\lambda Z} \int_{-\infty}^{+\infty} A_{DAO}(\mathbf{r}')\exp\left[-j\frac{k}{2}\left(\frac{|\mathbf{r}'|^2}{F} - \frac{|\mathbf{r} - \mathbf{r}'|^2}{L_i}\right)\right]d\mathbf{r}' \right|^2, \tag{7}$$

where k is the wave number, F is the focal length of the digital lens and $L_i = (1/F - 1/L)^{-1}$ is the distance between the digital lens plane and the image plane. The term L denotes the distance between the lens and the object plane of interest.

Step 3: Local image quality metric computation

The quality of the synthesized image $I_{DAO}(\mathbf{r})$ in Eq. (7) depends on the command vector $\mathbf{a}$ applied to the digital WFC [Eq. (5)]. Vector $\mathbf{a}$ can be considered as a parameter controlling the quality of image $I_{DAO}(\mathbf{r})$. Improving image quality in the region Ω_j can be achieved by optimizing a sharpness metric J_{Ω_j} given by

$$J_{\Omega_j}(\mathbf{a}) = \frac{\int I_{DAO}^2(\mathbf{r}) M_{\Omega_j}(\mathbf{r})d\mathbf{r}}{\int I_{DAO}(\mathbf{r}) M_{\Omega_j}(\mathbf{r})d\mathbf{r}}, \tag{8}$$

Where $M_{\Omega_j}(\mathbf{r})$ is the function defining region Ω_j [see Eq. (4)]. Note that although the intensity-squared sharpness metric is commonly used, other criteria could be used to assess image quality such as a gradient-based metric or the Tenengrad criterion.

Step 4: Image quality metric optimization

Optimization of metrics J_{Ω_j} can be achieved using various numerical techniques. We consider for example metric optimization based on the stochastic parallel gradient descent (SPGD) control algorithm [40]. In accordance with this algorithm command vector $\mathbf{a}$ update rule is given at each iteration n by the following procedure:

$$a_k^{(n+1)} = a_k^{(n)} + \gamma^{(n)}\delta J_{\Omega_j}^{(n)}\delta a_k^{(n)} \text{ for } k = 1, \ldots, N_{DAO}, \tag{9}$$

where $\gamma^{(n)} > 0$ is a gain coefficient, $\delta J_{\Omega_j}{}^{(n)}$ is the metric response to small-amplitude random perturbations of control vector $\{\delta a_k^{(n)}\}$ applied simultaneously to all N_{DAO} DWFC control channels. The control channel updates are repeated until convergence of vector $\mathbf{a}$ toward a small vicinity of the stationary state. The number of iterations N_{it} required for convergence is defined from the common criterion

$$\varepsilon\left(n = N_{it}\right) = \frac{\left| J_{\Omega_j}^{(n)} - J_{\Omega_j}^{(n-1)} \right|}{J_{\Omega_j}^{(n)}} \le \varepsilon_0 \ll 1, \tag{10}$$

and the resulting control vector for compensation of region Ω_j, denoted $\mathbf{a}_{\Omega_j}$, corresponds to the vector obtained at the last iteration: $\mathbf{a}_{\Omega_j} = \mathbf{a}^{(n=N_{it})}$. Optimization over the entire image region Ω can be achieved by repeating sequentially steps 1 through 4 for each region Ω_j and results in a set of control vectors $\{\mathbf{a}_{\Omega_j}\}$.

In an ideal compensation scenario the DWFC phase $\varphi_{DAO}(\mathbf{r})$ resulting from the optimization process would compensate exactly the turbulence-induced phase aberration so that $\varphi_{DAO}(\mathbf{r}) = \varphi_{turb}(\mathbf{r})$ [see Eq. (2)]. In this ideal case only phase information related to the object being imaged remains in the compensated field: $\arg\left[A_{DAO}(\mathbf{r})\right] = \varphi_{obj}(\mathbf{r})$ and leads to optimal image quality.

3. Performance analysis

In this section performance of DAO systems is analyzed using a numerical simulation and results for various system configurations and turbulence strengths are discussed.

3.1. Numerical model

Performance was evaluated from an ensemble of digitally-generated random complex-fields used as input optical waves to the DAO system. For each realization of the input field the complex amplitude in the DAO system pupil plane $A_{in}(r)$ (see Fig. 1) was obtained using the conventional split-operator approach for simulating wave optics propagation through a volume of atmospheric turbulence [41]. At the beginning of the propagation path ($z = 0$) we used a monochromatic optical field with complex amplitude $A_{prop}(\mathbf{r}, z = 0) = I_{obj}^{1/2}(\mathbf{r}) \exp\left[j \varphi_{surf}(\mathbf{r})\right]$, where $I_{obj}(\mathbf{r})$ is the intensity distribution of the object being imaged and $\varphi_{surf}(\mathbf{r})$ is a random phase function uniformly distributed in $[-\pi, \pi]$ and δ-correlated in space. The term $\varphi_{surf}(\mathbf{r})$ is used to model the "optically rough" surface of the object. The optical field complex amplitude at the end of the propagation path ($z = L$) was utilized as the DAO system input field: $A_{in}(\mathbf{r}) = A_{prop}(\mathbf{r}, z = L)$. Optical inhomogeneities along the propagation path were modeled with a set of 10 thin random phase screens correspond-

ing to the Kolmogorov turbulence power spectrum. We considered a horizontal propagation scenario so the phase screens were equally spaced along the propagation path and their impact (i.e. turbulence strength) was characterized by a constant ratio D/r_0 where D is the diameter of the DAO system aperture and r_0 is the characteristic Fried parameter for plane waves. By modifying ratio D/r_0 one can control the strength of input field phase aberrations. In the numerical simulations, D/r_0 ranged from zero (i.e. free-space propagation) to 10. Figures 3(a)-3(d) show examples of the input field intensity and phase distributions that are obtained using the technique described above for $D/r_0=4$ [(a) and (b)] and for $D/r_0=8$ [(c) and (d)]. Note that the phase distributions in Figs. 3(b) and 3(d) contain phase discontinuities (branch points). Images were obtained for a propagation distance $L=0.05L_{diff}$ where $L_{diff}=k(D/2)^2$ is the diffractive distance, $k=2\pi/\lambda$ is the wave number, and λ is the imaging wavelength.

The strength of the input field intensity scintillations was characterized by the aperture-averaged scintillation index σ_I^2 given by

$$\sigma_I^2 = \frac{1}{S}\int\left\{\frac{\langle[I(\mathbf{r})]^2\rangle}{\langle I(\mathbf{r})\rangle^2} - 1\right\}d^2\mathbf{r}, \qquad (11)$$

where $I(\mathbf{r})=|A_{in}(\mathbf{r})|^2$ and S is the aperture area of the DAO system. Here $<>$ denotes averaging over an ensemble of input fields corresponding to statistically independent realizations of the phase screens as well as the object roughness phase function $\varphi_{surf}(\mathbf{r})$. In the numerical simulations, ensemble averaging was performed over 100 sets of phase screens and object phases. Both intensity distributions in Figs. 3(a) and 3(c) are characterized by strong scintillations with an average scintillation index value of 1.

In the DAO system, digital wavefront compensation function $\varphi_{DAO}(\mathbf{r})$ is computed as a weighted sum of response functions $S_k(\mathbf{r})$ [see Eq. (5)]. In our numerical simulation these response functions are taken as scaled Zernike polynomials: $S_k(\mathbf{r})=Z_k(Q\mathbf{r})$, where $Z_k(\mathbf{r})$ is the Zernike polynomial with index k and Q is a scaling factor. Since Zernike polynomials are defined onto the unit circle the term Q is chosen as $Q=D/2$ so that response functions $S_k(\mathbf{r})$ are defined over the aperture area of the DAO system. In the numerical analysis we used $N_{DAO}=36$ Zernike polynomials corresponding to the first 8 Zernike modes. It should be noted that the first Zernike polynomial (piston) does not impact image quality and does not need to be included in the construction of $\varphi_{DAO}(\mathbf{r})$. Similarly, Zernike polynomials with index $k=2$ and $k=3$ (tip and tilt) do not have an influence on image quality or its metric. However, tip-tilt wavefront aberrations in the pupil plane cause a global shift of the intensity distribution in the image plane. In order to compensate for this, image alignment is performed in our numerical simulations by mean of a conventional registration technique [42] using an ensemble average image as a reference.
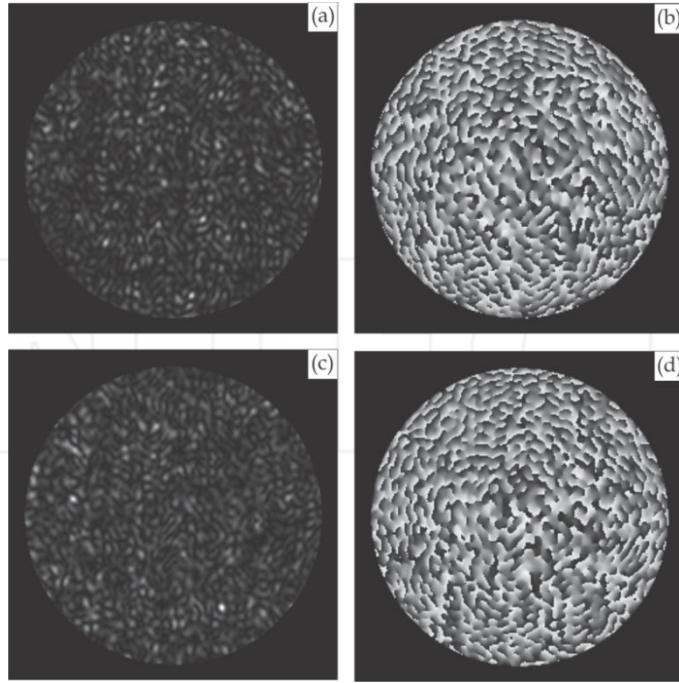
Figure 3. Intensity (left column) and phase (right column) distributions of the computer-generated complex field $A_{in}(\mathbf{r})$ used as input of the DAO system for $D / r_0 = 4$ [(a),(b)] and $D / r_0 = 8$ [(c),(d)]. Phase distributions are shown in a 2π range [between $-\pi$ (black) and $+\pi$ (white)].

The quality of the DAO-compensated image $I_{DAO}(\mathbf{r})$ is assessed using a sharpness metric defined as

$$J = \frac{\int I_{DAO}^2(\mathbf{r}) d\mathbf{r}}{\int I_{dl}^2(\mathbf{r}) d\mathbf{r}}, \tag{12}$$

Where $I_{dl}(\mathbf{r})$ is the image that would be obtained in the absence of atmospheric turbulence (i.e. diffraction-limited image). In the case of an ideal compensation the turbulence-induced wavefront aberrations are fully corrected by the DWFC [$\varphi_{DAO}(\mathbf{r}) = \varphi_{turb}(\mathbf{r})$] and $J = 1$.
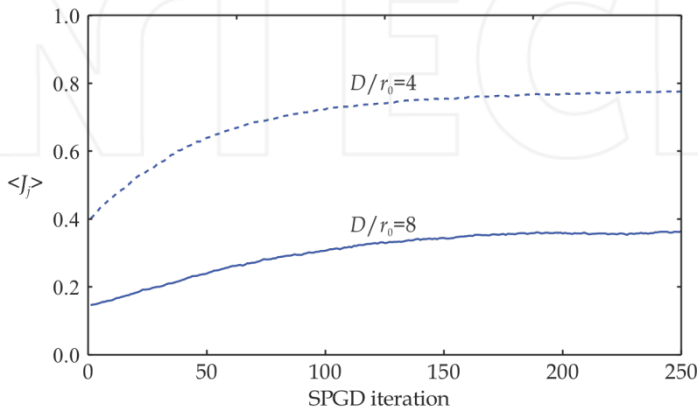
3.2. DAO system performance

In this section we analyze results of image synthesis and compensation using the DAO approach described in section 2 using the numerical model presented in section 3.1. In order to illustrate the effect of anisoplanatism we first consider DAO performance over an image region Ω_j that is nearly isoplanatic in size. Later we consider processing of the entire image region Ω (anisoplanatic conditions). Figure 4 shows intensity distribution $I_{DAO}(\mathbf{r})$ and cross-

sections for an object with intensity distribution consisting of point sources arranged in a 7-by-7 array. The resulting intensity distributions hence correspond to the average DAO-compensated PSF of the system for different values of the field angle θ, and is showed for $D/r_0=4$ [Figs. 4(a) and 4(b)] and for $D/r_0=8$ [Figs. 4(c) and 4(d)]. As a result of anisoplanatism the PSF is space-varying and its distribution broadens significantly as the angular separation θ with the metric region Ω_j increases. Also, the degradation occurs more rapidly with respect to angle θ as turbulence strength increases [compare cross-sections in Figs. 4(b) and 4(d)]. Results were obtained by averaging the resulting images $I_{DAO}(\mathbf{r})$ for 100 realizations of the random phase screens.
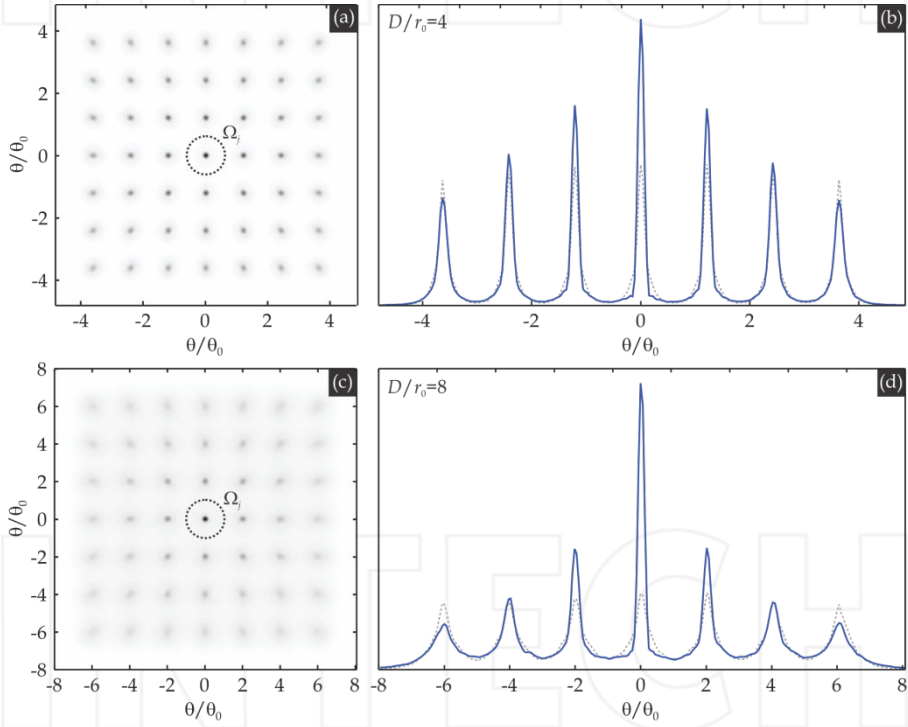
Figure 4. Average DAO-compensated intensity distributions (left column) for an array of 7-by-7 point sources for $D/r_0=4$ (top row) and $D/r_0=8$ (bottom row). The column on the right depicts the average uncompensated (dotted curve) and DAO-compensated (solid curve) cross-sections of the PSF's through the center of region Ω_j. Image compensation is based on optimizing image quality metric J_j defined over region Ω_j. Region Ω_j has a diameter ω_Ω of approximately $1.2\theta_0$ and $2\theta_0$ for $D/r_0=4$ and $D/r_0=8$ respectively (see circled areas).

As described in section 2.4 compensation is based on the optimization of metric J_j using an iterative SPGD algorithm. Figure 5 shows average convergence curves for metric J_j as a function of the number of SPGD iterations performed. The two curves displayed correspond to the optimization of image regions Ω_j shown in Figure 4 for $D/r_0=4$ and $D/r_0=8$. In both cases the metric value approximately doubled during the optimization process.


Figure 5. Average convergence curves for metric J_j. The curves displayed correspond to optimization of image region Ω_j shown in Fig. 4 for $D/r_0=4$ and $D/r_0=8$.

We consider now the performance of DAO systems under anisoplanatic conditions. Figures 6 and 7 display images prior and after DAO compensation for the point source object used in Figure 4 and for an USAF resolution chart respectively. Results are shown for two turbu‐ lence conditions: $D/r_0=4$ and $D/r_0=8$ and correspond to a full field-of-view of approxi‐ mately $10\theta_0$ and $16\theta_0$. In both Figures significant image quality improvements can be observed with an increase of the metric J of 70% (point source object) and 49% (USAF ob‐ ject) for $D/r_0=4$, and 123% and 33% for $D/r_0=8$.

The performance of the DAO compensation technique with respect to turbulence strength is illustrated in Fig. 8 for a ratio D/r_0 in the range [0;10]. Within that range the average image quality metric $\langle J \rangle$ after compensation always exceeds significantly the metric value prior processing. Image quality improvements become especially important for large D/r_0. For example, for $D/r_0=10$ the metric grew by a factor of nearly 3. Plots showed in Fig. 8 and in the remainder of the chapter as shown for the object consisting of an array of point sources as depicted in Fig. 6.
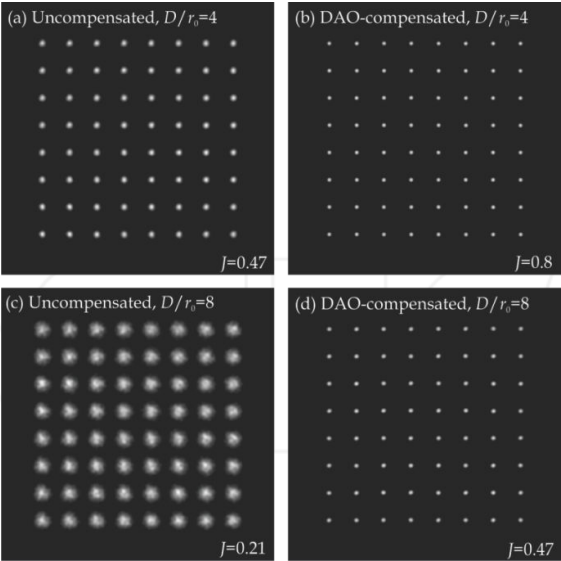
Figure 6. Image of an array of point sources prior and after anisoplanatic DAO compensation for $D/r_0=4$ (top row) and $D/r_0=8$ (bottom row).
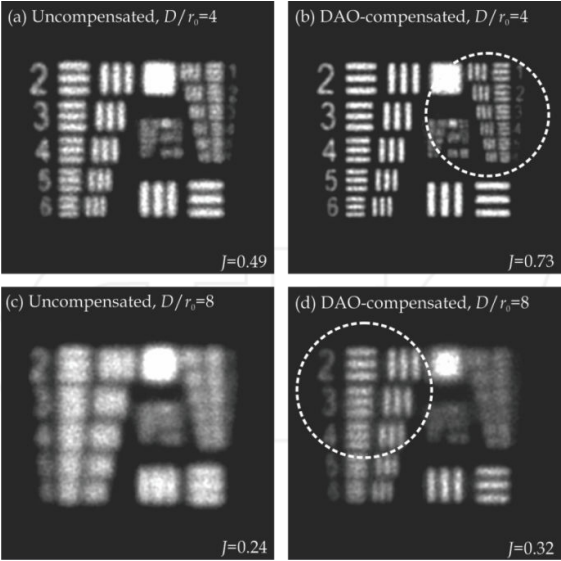

Figure 7. Image of an USAF resolution chart prior and after anisoplanatic DAO compensation for $D/r_0=4$ and $D/r_0=8$. Note that the DAO compensation process reveals image details as pointed out by the circled areas.
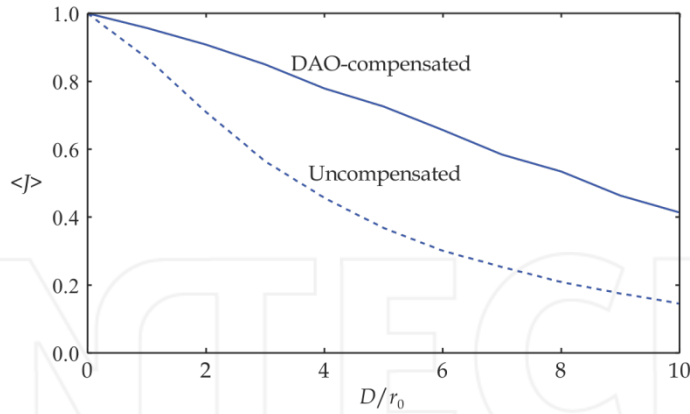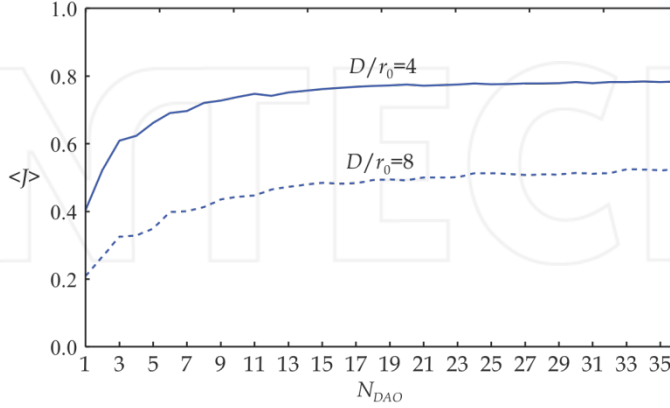
Figure 8. Average image quality metric $\langle J \rangle$ as function of the turbulence strength characterized by the ratio D / r_0 with and without DAO compensation.

As mentioned in section 1.3 anisoplanatism causes compensation approaches based on single phase conjugation to be effective only over a small angle of size related to the isoplanatic angle θ_0. As a result the block-by-block processing technique used here performs differently as the size ω_Ω of blocks Ω_j changes. As shown in Fig. 9 DAO performance degrades noticeably as ω_Ω increases. For example we have $\langle J \rangle$=0.73 for ω_Ω=1.8θ_0 and $\langle J \rangle$=0.44 for ω_Ω=14θ_0. This illustrates the efficiently of the block-by-block processing technique to mitigate the anisoplanatic effect.
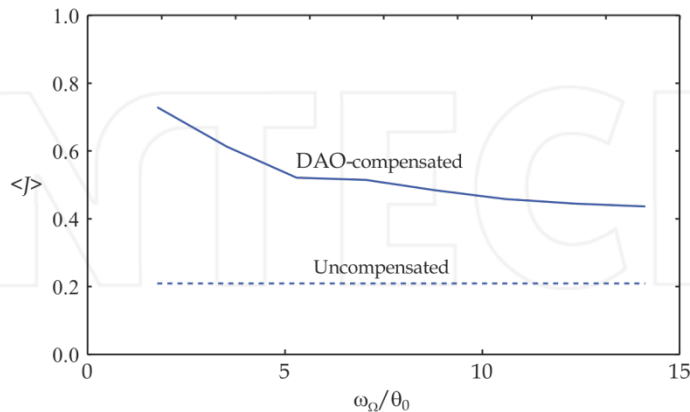
Figure 9. Average image quality metric $\langle J \rangle$ as a function of the diameter ω_Ω of region Ω_j used for metric computation.

Finally the influence of the number of Zernike polynomials N_{DAO} compensated [see Eq. (5)] is shown in Fig. 10 for two turbulence strength levels: $D/r_0=4$ and $D/r_0=8$. Image quality improvements become negligible beyond a threshold for parameter N_{DAO}. This threshold is in the range of $[10;20]$ for $D/r_0=4$ and $[15;25]$ for $D/r_0=8$.

Figure 10. Average image quality metric $\langle J \rangle$ as a function of the degree of DAO compensation N_{DAO}.

4. Conclusion

We introduced in this chapter an alternative technique to conventional adaptive optics imaging schemes which we refer to as digital adaptive optics. The technique consists in a two-step process. First, an optical sensor provides a measurement of the wave's complex-amplitude (intensity and phase distributions) in the pupil of the imaging system. This differs from the conventional AO approach in which typically only the wavefront is sensed. Second, digital post-processing algorithms are applied to the complex-field measurements in order to synthesize an image and mitigate the effect of atmospheric turbulence. This final step is based on the optimization of an image quality metric and compensation of the wavefront aberrations is performed in a numerical manner. While the conventional AO approach compensates aberrations in real-time the DAO operates as a post-processing scheme. DAO systems has the advantage of requiring simpler and less costly implementations since they do not require opto-mechanical wavefront correctors and their real-time control hardware, but this also means they are primarily suited for applications that do not require real-time operation.

Performance of DAO systems was evaluated by mean of a numerical analysis. The analysis revealed the DAO approach can significantly improve image quality even in strong turbulence conditions. The block-by-block processing technique presented was shown to be effec-

tive for image synthesis and compensation under anisoplanatic scenarios. The influence of the block size on DAO performance was showed to enhance performance as the block size decreases and nears values of the isoplanatic angle. Finally, increasing the degree of DAO compensation (i.e. number of Zernike coefficients compensated) was showed to benefit performance up to a threshold value which depends on the turbulence strength.

Author details

Mathieu Aubailly[1*] and Mikhail A. Vorontsov[2]

*Address all correspondence to: mathieu@umd.edu

1 Intelligent Optics Laboratory, Institute for Systems Research, University of Maryland, College Park, Maryland, USA

2 Intelligent Optics Laboratory, School of Engineering, University of Dayton, Dayton, Ohio, USA

References

[1] J. W. Hardy, *Adaptive Optics for Astronomical Telescopes* (Oxford University, 1998).

[2] R. Tyson, *Principles of Adaptive Optics*, Third Edition (CRC Press, 2010).

[3] J. Porter, H. Queener, J. Lin, K. Thorn, A. A. S. Awwal, *Adaptive Optics for Vision Science: Principles, Practices, Design and Applications* (Wiley, 2006).

[4] M. C. Roggemann and B. M. Welsh, *Imaging Through Turbulence* (CRC-Press, 1996).

[5] B. M. Welsh and C. S. Gardner, "Performance analysis of adaptive-optics systems using laser guide stars and slope sensors," J. Opt. Soc. Am. A 6, 1913-1923 (1989).

[6] B. M. Welsh and L. A. Thompson, "Effects of turbulence-induced anisoplanatism on the imaging performance of adaptive-astronomical telescopes using laser guide stars," J. Opt. Soc. Am. A 8, 69–80 (1991).

[7] D. L. Fried, "Anisoplanatism in adaptive optics," J. Opt. Soc. Am. 72, 52–61 (1982).

[8] J. Christou, E. Steinbring, S. Faber, D. Gavel, J. Patience, and E. Gates, "Anisoplanatism within the isoplanatic patch," Am. Astron. Soc. 34, 1257 (2002).

[9] D. C. Johnston and B. M. Welsh, "Analysis of multiconjugate adaptive optics," J. Opt. Soc. Am. A 11, 394–408 (1994).

[10] B. L. Ellerbroek, "First-order performance evaluation of adaptive optics systems for atmospheric turbulence compensation in extended field of view astronomical telescopes," J. Opt. Soc. Am. A 11, 783–805 (1994).

[11] T. Fusco, J.-M. Conan, G. Rousset, L. M. Mugnier, and V. Michau, "Optimal wavefront reconstruction strategies for multiconjugate adaptive optics," J. Opt. Soc. Am. A 18, 2527–2538 (2001).

[12] M. Lloyd-Hart, C. Baranec, N. M. Milton, M. Snyder, T. Stalcup, and J. R. P. Angel, "Experimental results of ground-layer and tomographic wavefront reconstruction from multiple laser guide stars," Opt. Express 14, 7541-7551 (2006).

[13] M. Aubailly, M. C. Roggemann, and T. J. Schulz, "Approach for reconstructing anisoplanatic adaptive optics images," Appl. Opt. 46, 6055-6063 (2007).

[14] J. D. Barchers, D. L. Fried, and D. J. Link, "Evaluation of the performance of Hartmann sensors in strong scintillation," Appl. Opt. 41, 1012–1021 (2002).

[15] F. Roddier, "Curvature sensing and compensation: a new concept in adaptive optics," Appl. Opt. 27, 1223–1225 (1988).

[16] G. Rousset, "Wave-front sensors," in *Adaptive Optics in Astronomy*, F. Roddier, ed. (Cambridge University, 1999), pp. 91–130.

[17] R. W. Gerchberg and W. O. Saxton, "A practical algorithm for the determination of phase from image and diffraction plane pictures," Optik 35, 237–246 (1972).

[18] J. R. Fienup, "Phase retrieval algorithms: a comparison," Appl. Opt. 21, 2758-2769 (1982).

[19] V. Yu. Ivanov, V. P. Sivokon, and M. A. Vorontsov, "Phase retrieval from a set of intensity measurements: theory and experiment," J. Opt. Soc. Am. A 9, 1515-1524 (1992).

[20] R. A. Gonsalves, "Phase retrieval from modulus data," J. Opt. Soc. Am. 66, 961–964 (1976).

[21] R. G. Paxman and J. R. Fienup, "Optical misalignment sensing and image reconstruction using phase diversity," J. Opt. Soc. Am. A 5, 914–923 (1988).

[22] M. A. Vorontsov, E. W. Justh, and L. A. Beresnev, "Adaptive optics with advanced phase-contrast techniques. I. High-resolution wave-front sensing," J. Opt. Soc. Am. A 18, 1289-1299 (2001).

[23] E. W. Justh, M. A. Vorontsov, G. W. Carhart, L. A. Beresnev, and P. S. Krishnaprasad, "Adaptive optics with advanced phase-contrast techniques. II. High-resolution wave-front control," J. Opt. Soc. Am. A 18, 1300-1311 (2001).

[24] F. Zernike, "How I discovered phase contrast," Science 121, 345–349 (1955).

[25] J. W. Goodman, *Introduction to Fourier Optics* (McGraw-Hill, New York, 1996).

[26] S. A. Akhmanov and S. Yu. Nikitin, *Physical Optics* (Clarendon, Oxford, UK, 1997).

[27] R. N. Smartt and W. H. Steel, "Theory and application of point-diffraction interferometers," Jpn. J. Appl. Phys. 14, 351–356 (1975).

[28] P. Hariharan, ed., *Selected Papers on Interferometry* (SPIE Optical Engineering Press, Bellingham, Wash., 1991).

[29] R. Angel, ''Ground-based imaging of extrasolar planets using adaptive optics,'' Nature 368, 203–207 (1994).

[30] K. Underwood, J. C. Wyant, and C. L. Koliopoulos, ''Selfreferencing wavefront sensor,'' in Wavefront Sensing, N. Bareket and C. L. Koliopoulos, eds., Proc. SPIE 351, 108–114 (1982).

[31] J. C. Marron, R. L. Kendrick, N. Seldomridge, T. D. Grow, and T. A. Höft, "Atmospheric turbulence correction using digital holographic detection: experimental results," Opt. Express 17, 11638-11651 (2009).

[32] A. E. Tippie and J. R. Fienup, "Multiple-plane anisoplanatic phase correction in a laboratory digital holography experiment," Opt. Lett. 35, 3291-3293 (2010).

[33] N. J. Miller, J. W. Haus, P. F. McManamon, D. Shemano, "Multi-aperture coherent imaging," Proc. SPIE 8052 (2011).

[34] M. Aubailly and M. A. Vorontsov, "Scintillation resistant wavefront sensing based on multi-aperture phase reconstruction technique," J. Opt. Soc. Am. A 29, 1707-1716 (2012).

[35] V. U. Zavorotnyi, "Strong fluctuations of the wave intensity behind a randomly inhomogeneous layer," Radiophys. Quantum Electron. 22, 352–354 (1979).

[36] M. C. Rytov, Yu A. Kravtsov, and V. I. Tatarskii, eds., Principles of Statistical Radiophysics 4, *Wave Propagation Through Random Media* (Springer-Verlag, 1989).

[37] L. C. Andrews, R. L. Phillips, C. Y. Hopen, and M. A. Al-Habash, "Theory of optical scintillation," J. Opt. Soc. Am. A 16, 1417–1429 (1999).

[38] D. L. Fried, "Branch point problem in adaptive optics," J. Opt. Soc. Am. A 15, 2759–2768 (1998).

[39] D. L. Fried and J. L. Vaughn, "Branch cuts in the phase function," Appl. Opt. 31, 2865–2882 (1992).

[40] M. A. Vorontsov and V. P. Sivokon, "Stochastic parallel-gradient-descent technique for high-resolution wave-front phase-distortion correction," J. Opt. Soc. Am. A 15, 2745–2758 (1998).

[41] J. A. Fleck, J. R. Morris, and M. D. Feit, "Time-dependent propagation of high energy laser beams through the atmosphere," Appl. Phys. 10, 129–160 (1976).

[42] E. De Castro and C. Morandi, "Registration of translated and rotated images using finite Fourier transforms," IEEE Trans. Pattern Analysis and Machine Intelligence 9, 700–703 (1987).